Computational Materials Science 199 (2021) 110716

Contents lists available at ScienceDirect

Computational Materials Science

journal homepage: www.elsevier.com/locate/commatsci

The influence of defects on the elastic response of lattice structures resulting from additive manufacturing

Panwei Jiang [a], Edward C. De Meter [b], Saurabh Basu [b,*]

[a] Department of Materials Science and Engineering, Pennsylvania State University, State College 16802, Pennsylvania, USA
[b] Harold and Inge Marcus Department of Industrial and Manufacturing Engineering, Pennsylvania State University, University Park 16802, Pennsylvania, USA

ARTICLE INFO

Keywords:
Additive manufacturing
Lattice structure
Manufacturing defect
Gibson-Ashby model
Finite element method
Bayesian inferencing

ABSTRACT

Stiffness prediction for additively manufactured (AM) lattices is necessary for lightweight components design. For a given lattice structure, the Gibson and Ashby (GA) model can predict relative stiffness as a function of its relative density. However, volumetric porosity and surface roughness defects that are commonplace in AM lattices depreciate the quality of prediction made by the GA model. This is because such defects complicate the elastic behavior of lattice structures. In this work, a modified GA model is proposed that accounts for these defects. A Bayesian inferencing framework is constructed to delineate the influence of spatial distributions of these defects on resulting mechanical response. Principal component analysis (PCA) is used to identify differences between elastic strain fields (ϵ_{11}, ϵ_{22}, and ϵ_{12}) resulting from perfect and defective lattices. The insights obtained can provide a viable approach to predict the mechanical response of as-received AM lattices that are often defective, and thereby enable systematic approaches for their design.

1. Introduction

Complex lattice structures with high strength-to-weight ratios that could not be produced via traditional routes can now be fabricated by additive manufacturing (AM). The circumvention of several design for manufacturing issues via AM has spurred rapid innovation aimed towards highly beneficial functional behavior in these structures. However, layer-by-layer fabrication in AM naturally results in volumetric porosity and surface roughness defects [1–8] that can compromise the performance of these structures. This shortcoming can be mitigated by post-processing involving hot-isostatic pressing (HIP), e.g., for eradicating volumetric defects, and super-finishing, e.g., for eradicating surface roughness. Unfortunately, both of these families of post-processing steps are only partially efficient, wherein a certain fraction of defects can be expected to be present in high-performance lattice structures resulting from AM [9–11]. This is of serious concern, especially in thin-walled structures where even small densities of defects can rapidly compromise performance. Recent efforts have attempted to create methodologies using advanced numerical simulations [12,13], and machine learning algorithms [14,15] that attempt to accelerate computational predictions of the influence of the aforementioned defects. The overarching goal of these efforts is to carefully permit acceptable defect densities without risking premature failure. The fundamental influence of micro-scale defects on macro-scale lattice structures is however not well understood. The traditional approach towards modeling the mechanics of lattice structures involves the use of the Gibson-Ashby equation in which the relative modulus of the structure $\frac{E^*}{E_s}$ is formulated as a function of its relative density $\frac{\rho^*}{\rho_s}$ as [8]:

$$\frac{E^*}{E_s} = C\left(\frac{\rho^*}{\rho_s}\right)^n \tag{1}$$

Here, E^* is the elastic modulus of the lattice structure, which is a function of its geometry and the elastic modulus E_s of its parent material. The bulk density of the parent material is given by ρ_s. The term ρ^* is the volumetric density of the structure. This is a design variable that can be characterized using geometrical details of the structure prior to manufacturing, thereby facilitating systematic light-weighting of mechanical parts. Finally, n, C are structure specific coefficients that characterize its mechanics in the absence of any defects. The original model which was rooted in the elastic mechanics of beam elements [16–18] has been applied with exceptional success in predicting the mechanics of many families of lattice structures [19]. However, this model is not equipped to directly encapsulate the influence of uncontrolled micro-scale defects that originate during manufacturing such as

* Corresponding author.
E-mail address: sxb514@psu.edu (S. Basu).

https://doi.org/10.1016/j.commatsci.2021.110716
Received 17 April 2021; Received in revised form 7 July 2021; Accepted 8 July 2021
Available online 26 July 2021

the porosity and surface roughness defects of AM [20].

In this work, the authors attempt to delineate fundamental linkages between volumetric porosity and surface roughness defects, and the resulting performance of lattice structures. The overarching goal of this work is to create a simple approach that can provide a first order prediction of this influence. In this regard, the present work can be highly impactful as a simple tool that can be used for designing complex lattice structures while accounting for defects which are expected during fabrication in a given manufacturing platform.

Towards this end, the effects of volumetric porosity and surface roughness defects on the mechanical response of 2.5D body centered cubic lattice structures is studied. In the first step, the mechanical response of a single 1×1 unit cell is studied numerically. Here, controlled numerical tests are performed to evaluate the exclusive influence of porosity and surface roughness defects. Subsequently, the combined effects of these defects on mechanical response is analyzed. This unit cell is shown in Fig. 1 and has a Maxwell number [4] $M = s_t - 2n_o + 3 = 6 - 2 \times 5 + 3 = -1$, where s_t, n_o refer to number of struts, and nodes in the structure, respectively. A Maxwell number $M < 0$ encourages bending dominant behavior in individual struts of the lattice structure upon application of compressive boundary conditions [19]. This naturally promotes instabilities in the mechanical response, especially when thin strut walls are used. The GA model predicts the mechanical response of defect-free bending dominant structures with $n = 2$ (Ref. Eq. (1)) [4,16]. In this regard, deviations of the mechanical response of the unit cell with respect to predictions made by the GA model due to the presence of manufacturing defects will provide a platform to delineate their influence.

2. Methods

2.1. Finite element framework

The Abaqus-Python interface was used to set up the plane stress finite element model. 2.5D lattice structures like the one shown in Fig. 1 were generated by specifying length $l_s = 4\ mm$, distance $d_s = 2.6\ mm$ between two inclined struts, thickness $t_{shell} = 0.4\ mm$ of the shell (e.g., top and bottom layer), and thickness t_{strut} of the struts. Table 1 summarizes these thickness parameters. Isotropic elastic material properties of

Table 1
Summary of lattice structure parameters.

Set #	Strut type	t_{strut} (mm)	porosity α	t_{min}/t_{max}
1	Smooth	0.1–1.0	–	1
2	Porosity defect- uniform	0.3	0.0511–0.1957	–
3	Porosity defect- uniform	0.4	0.0482–0.1125	–
4	Porosity defect- uniform	0.7	0.0283–0.1208	–
5	Porosity defect- uniform	1	0.0259–0.0791	–
6	Porosity defect- surface	0.3	0.0340–0.1957	–
7	Porosity defect- surface	0.4	0.0289–0.1286	–
8	Porosity defect- surface	0.7	0.0264–0.1075	–
9	Porosity defect- surface	1	0.0314–0.0791	–
10	Roughnenss defect	0.3	–	0.5789–0.9868
11	Roughnenss defect	0.4	–	0.6667–0.9900
12	Roughnenss defect	0.7	–	0.7949–0.9943
13	Roughness, uniform porosity	0.4	0.0482–0.1608	0.9608
14	Roughness, uniform porosity	0.4	0.0482–0.1672	0.8519

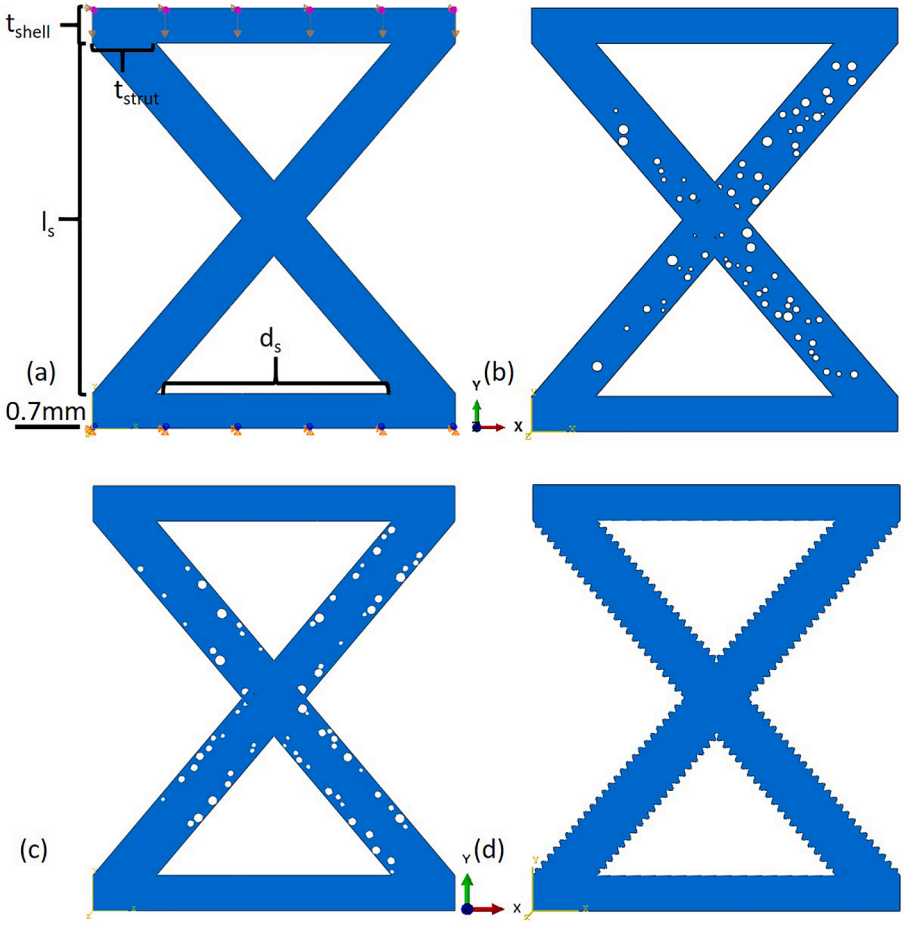

Fig. 1. (a) Lattice structure with no porosity and roughness on struts featuring parameters $t_{shell} = 0.4\ mm$, $l_s = 4\ mm$, $d_s = 2.6\ mm$, $t_{strut} = 0.7\ mm$. Boundary conditions are shown on bottom and top edges. (b) An instance of the lattice structure shown in Fig. 1(a) with 6% volumetric porosity defects that are uniformly distributed in the load bearing struts. (c) An analogue of the lattice shown in (b) but with defects concentrated near the surface of the struts. (d) The lattice structure in Fig. 1a instilled with sinusoidal surface roughness featuring amplitude $a = 28\ \mu m$, and wavelength $\lambda = 108\ \mu m$.

Inconel 718 were used in the model, viz. Young's modulus E = 212 GPa, and Poisson's ratio $\nu = 0.294$ [21]. The boundary conditions are shown in Fig. 1a. The bottom surface was fixed, and the top surface was compressed by 0.048 mm along y direction corresponding to a globally imposed compressive strain of 0.01. The global seed size for meshing was set at 4 μm. Circular porosity and sinusoidal surface roughness defects were implanted onto the inclined load bearing struts of the structures. The pores were generated by sampling radii uniformly from the range $20\ \mu m - 60\ \mu m$. Subsequently, their center positions were sampled in 2 different ways such that they were: (i) uniformly distributed within the thickness of the strut, and (ii) distributed within a band of thickness $0.2t_{strut}$ in the vicinity of the surface of the strut. These modalities were sampled to delineate the effect of changes in distributions of spatial locations of defects on mechanical response. The numerical implementation of this specimen generation step involved fixing the number of porosity defects and then sampling their diameters and spatial locations. Subsequently, the densities of defects in the parent material were characterized as $\alpha = \frac{\Sigma_i A_i}{A_{strut}}$, where A_i is the area of the *ith* defect, and A_{strut} is the total area of the 4 inclined load bearing struts (Ref. Fig. 1). In this implementation, the number of pores varied between 15, e.g. for strut parameter $t_{strut} = 0.3\ mm$, to 70, e.g., for strut parameter $t_{strut} = 1\ mm$. This resulted in volumetric porosity ranges between $\alpha = 0.02 - 0.2$ for various instances of numerical struts studied here, as summarized in Table 1. Fig. 1b shows an instance of the strut featuring parameter $t_{strut} = 0.7\ mm$ and a uniformly distributed volumetric porosity of $\alpha = 0.06$. Fig. 1c shows an instance of a strut of equal thickness, e.g., $t_{strut} = 0.7\ mm$, but with a porosity of $\alpha = 0.06$ distributed in the vicinity of the surface. Surface roughness defects were implanted onto the strut faces as sinusoidal waves of the form:

$$y = a\sin(2\pi\frac{x}{\lambda}) \tag{2}$$

, where a is the amplitude of the sine wave, λ is its wavelength, and y represents the deviation from the mean, i.e. smooth strut wall. Such a wave profile corresponds to a surface roughness measure of $R_a = \frac{2a}{\pi}$. Fig. 1d shows a lattice structure with parameter $t_{strut} = 0.7\ mm$ with sinusoidal surface roughness featuring parameters $a = 28\ \mu m$, $\lambda = 108\ \mu m$, corresponding to $R_a \approx 17.8\ \mu m$. Since the deviation of the surfaces with respect to their means does not produce an effective volume change, numerical surface roughness experiments were parameterized in this study as $\frac{t_{min}}{t_{max}}$, with the numerator and the denominator corresponding to the minimum and maximum thickness of a rough strut. In a lattice structure featuring a sinusoidal roughness profile as give in Eq. (2), this parameter approximates to $\frac{t_{strut}-2a}{t_{strut}+2a} \approx 1 - \frac{4a}{t_{strut}}$, when $a \ll t_{strut}$. The deformation of these lattices was simulated using the Abaqus-implicit compiler. Multiple instances of every lattice structure were studied, as summarized in Table 1. Following the simulations, various parameters including reaction force vs. displacement curve, and strain field components were extracted. The reaction force was converted to relative elasticity modulus (e.g., parameter $\frac{E^*}{E_s}$ in Eq. (1)). Dataset 1 was utilized for calibrating the GA model that would be applicable to our 2.5D BCC structures. Dataset 2–9, and 10–12, were utilized for delineating the effect of porosity, and roughness defects, respectively. Subsequently, the deformation of more complex lattice structures under the simultaneous influence of both porosity and surface roughness defects was also studied, e.g., those summarized as datasets 13–14 in Table 1.

2.2. Principal component analysis

Principal component analysis (PCA) was used to delineate the differences between strain fields expressed by various numerical strut specimens. PCA can enable classification of mechanical response datasets based on their salient characteristics that are influenced by defects in the parent lattice structure. The primary purpose of this PCA was to demonstrate that porosity and surface roughness defects fundamentally alter the mechanical response of lattice structures, which then merits alterations to the GA model for their encapsulation. Towards this end, strain fields expressed by various lattice structures, e.g. 2–5 (uniform defects), and 10–12 (roughness defects) in Table 1 when subject to the same boundary conditions were used as a metric of their mechanical response. It was realized that a direct analysis of strain fields for this purpose can produce erroneous insights as the strain field itself is sensitive to the exact configuration of defects. To mitigate this, PCA was performed on the Fourier representation of the auto-correlation function, separately on the three independent components of the strain field, viz. $\epsilon_{11}, \epsilon_{22}, \epsilon_{12}$. The auto-correlation function is defined as:

$$f_{ijij}(\underset{\sim}{\tau}) = \int_{\Omega} \epsilon_{ij}(\underset{\sim}{r})\epsilon_{ij}(\underset{\sim}{r}+\underset{\sim}{\tau})d\underset{\sim}{r} \tag{3}$$

Here, Ω refers to the domain of the these strain field components. This calculation is facilitated using the Fourier transform as [22]:

$$\mathcal{F}(f_{ijij}) = \mathcal{F}(\epsilon_{ij})\overline{\mathcal{F}}(\epsilon_{ij}) \tag{4}$$

where $\mathcal{F}$ refers to the Fourier transform, and $\overline{\mathcal{F}}$ is its conjugate. The auto-correlation of a field is often used to characterize its self similarity, and its Fourier representation eliminates phase information from it, thus making it rotationally invariant. It is hypothesized that this representation of a strain field captures the influence of defects in the parent material in a form that is insensitive to 'minor' defect-microstructure changes. The implementation of the PCA involved setting of the aforementioned domains as rectangular windows centrally located within load bearing struts of 1×1 dimensional lattice structures as shown in Fig. 2. The width of these rectangular domains was 0.2 mm. A collection of 64, 44 domains were extracted from lattice structures featuring porosity, and roughness defects, respectively. The analysis was done separately for specimens exhibiting porosity and those exhibiting roughness. This involved obtaining a set of uncorrelated variables with ordered variance (from max to min) through PCA of parameters $\mathcal{F}(f_{ijij})$, with $ij = 11, 22, 12$, respectively. The principal components of the parameter $\mathcal{F}(f_{ijij})$ were obtained as the eigen vectors **V** of the covariance **S** of the matrix $[\mathcal{F}_{n,1}(f_{ijij})^* \mathcal{F}_{n,2}(f_{ijij})^* \mathcal{F}_{n,3}(f_{ijij})^* \ldots \mathcal{F}_{n,2}(f_{ijij})^*]$ of the zero centered parameters $\mathcal{F}_{n,s}(f_{ijij})^* = \mathcal{F}(f_{ijij}) - [\mathcal{F}(f_{ijij})]$ corresponding to the aforementioned $s = 64, 44$ samples in their columnar forms, where n denotes the dimensionality of the strain query windows shown in Fig. 2. [23].

3. Results and discussions

3.1. Calibration of Gibson-Ashby model for 2.5D BCC lattice structure

The mechanics of defect-free 1×1 dimensional unit cells were characterized by creating these structures in Abaqus using its Python interface, and simulating their elastic deformation to a global compressive strain of 0.01. For creating these lattices, structure parameters $t_{strut} \in \{0.1, 0.2, \cdots 1\ mm\}$ were used. Subsequently, the force vs. displacement curves were extracted from these simulations, which were then converted to relative moduli $\frac{E^*}{E_s}$. These relative moduli were then plotted with respect to corresponding relative densities $\frac{\rho^*}{\rho_s}$, that were characterized as the area fractions of the boxes enclosing the lattice structure that are occupied by strut material, i.e. $\frac{\rho^*}{\rho_s} = \frac{\rho^*(t_{strut})+\rho_{shell}}{\rho_s}$. Here, $\frac{\rho^*(t_{strut})}{\rho_s}$ is the relative density of the inclined load bearing strut, which is a function of the strut thickness t_{strut}, and $\frac{\rho_{shell}}{\rho_s}$ is the relative density of the two horizontal, e.g. bottom and top shell walls (Ref. Fig. 1) and is constant ($\frac{\rho_{shell}}{\rho_s} = 0.167$) throughout this work. Fig. 3 shows results of this exercise. By fixing the coefficient $n = 2$, the mechanical behavior of the BCC family of lattice structures was characterized via the GA model

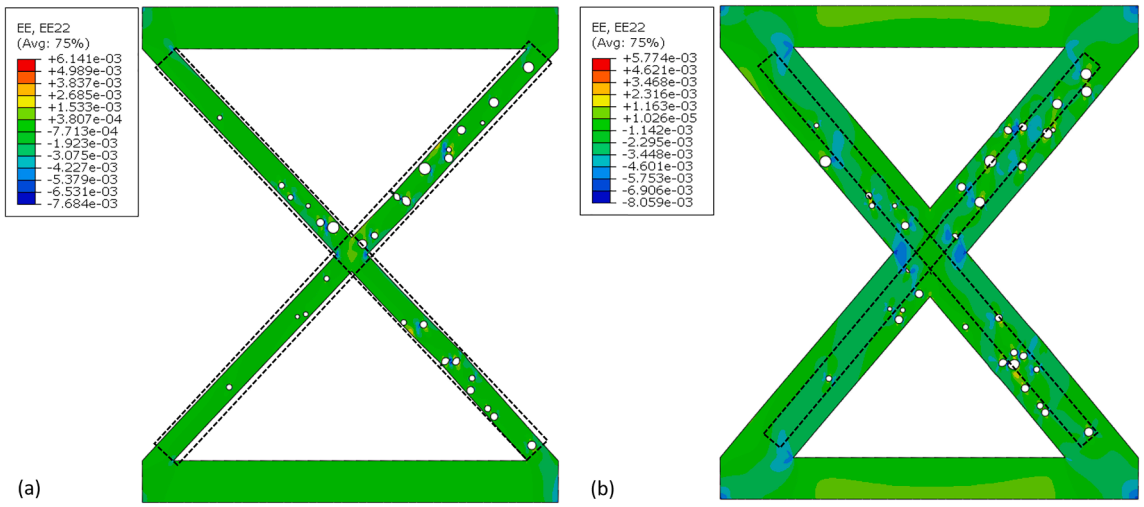

Fig. 2. Query window to extract (a) EE22 (ϵ_{22}) in lattice with $t_{strut} = 0.3\ mm$, (b) EE22 (ϵ_{22}) in lattice with $t_{strut} = 0.7\ mm$.

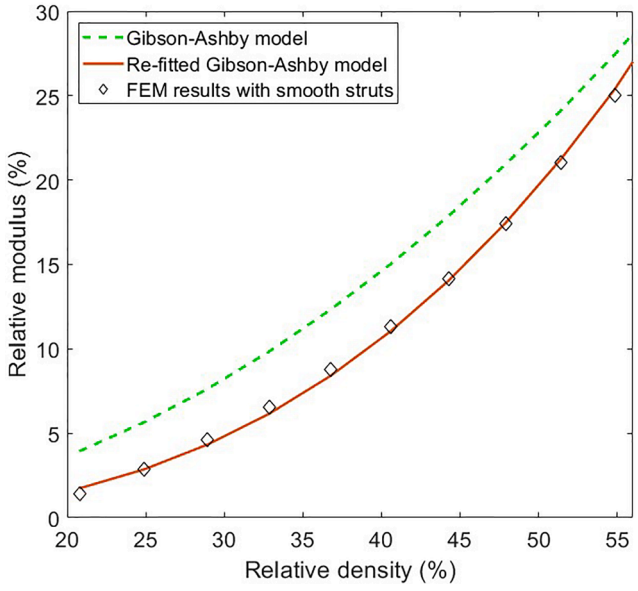

Fig. 3. Variation of numerically simulated relative elastic moduli $\frac{E^*}{E_s}$ with respect to relative density $\frac{\rho^*}{\rho_s}$.

using coefficients $C = 0.912$. This is shown using the green dashed line in Fig. 3, which clearly exhibits deviations with respect to the plane stress BCC lattice structure studied here. Nonetheless, a re-fitted GA model with coefficients $C = 1.334$, $n = 2.763$ as shown using the orange curve is able to capture the behavior of the defect free BCC lattice. It is noteworthy that the GA exponent of our plane-stress BCC lattice structure, e.g., n = 2.763, falls in close vicinity of the 3D BCC lattice structure, e.g., n = 2.84, as documented in Ref. [24].

3.2. The effect of porosity defects on mechanical response of lattice structures

The effect of porosity defects on the mechanical response of lattice structures was characterized by implanting numerical voids into struts followed by numerical simulation of their deformation. Subsequently, force vs. displacement profiles were extracted from these simulations. In turn, these were converted to relative moduli $\frac{E^*}{E_s}$. Figs. 4a–c show the von-Mises stress fields of a lattice with struts of thickness $t_{strut} = 0.4\ mm$, featuring uniformly distributed porosity defects at fractions of $\alpha = 0$, 0.0450, and 0.0965, respectively. Compared with the defect free lattice structure seen in Fig. 4a, the defective structures in Figs. 4b, c exhibit a complex stress field. To quantify the degradation of stiffness due to the presence of porosity defects, their relative moduli were characterized as functions of their process induced relative densities which are formulated as: $\frac{\rho^*(\alpha)}{\rho_s} = \frac{\rho^*(t_{strut})(1-\alpha)+\rho_{shell}}{\rho_s}$, where α is the density of the numerically simulated process induced defects. This enables a comparison between a defect free lattice structure, e.g., that featuring the a priori designed relative density $\frac{\rho_1^*}{\rho_s} = \frac{\rho^*(t_{strut})+\rho_{shell}}{\rho_s}$ with another defective lattice featuring relative density $\frac{\rho_2^*}{\rho_s} = \frac{\rho^*(t_{strut})(1-\alpha)+\rho_{shell}}{\rho_s}$. Figs. 4d–g illustrate this analysis for lattice structures featuring $t_{strut} = 0.3\ mm, 0.4\ mm, 0.7\ mm, 1\ mm$, these featuring designed relative density parameters $\frac{\rho_1^*}{\rho_s} = 0.2890, 0.3290, 0.4430, 0.5480$, respectively.

With respect to their defect-free counterparts, the struts featuring defects exhibited degradation of their mechanical response $\frac{E^*}{E_s}$ at remarkably larger rates than an a priori designed decrease in strut thickness would produce, e.g., that is encapsulated in the GA model (ref Eq. (1)). For instance, a relative decline of $\sim$ 48%, 35.4%, 30.1%, 23.2% was seen in the relative moduli $\frac{E^*}{E_s}$ for $\Delta\frac{\rho^*}{\rho_s} = 3.2\%$ resulting from porosity defects, compared with defect free counterparts that exhibited smaller levels of decline 21%, 15.4%, 20.4%, 12.8% from a pure reduction in strut thickness, respectively. Although a monotonic change in the rate of this decline was not observed as a function of the respective strut thicknesses, it is evident from these observations that characteristics of the decline were influenced by the mechanics of the original defect-free strut. This observation is formulated phenomenologically as an influence of the defect fraction α on the ratio β between observed mechanical response $\frac{E^*}{E_s}$ and that predicted by the GA model $C\left(\frac{\rho^*}{\rho_s}\right)^n$ as:

$$\frac{d\beta}{d\alpha} = -\kappa\beta \tag{5}$$

$$\text{where, } \beta = \frac{\frac{E^*}{E_s}}{C\left(\frac{\rho^*}{\rho_s}\right)^n} \tag{6}$$

Here, κ is a fitting coefficient that encapsulates the influence of the mechanics of the parent defect-free strut. Taking the integral of the Eq. (6) and upon rearranging, we get:

$$\beta = C' e^{-\kappa\alpha} \tag{7}$$

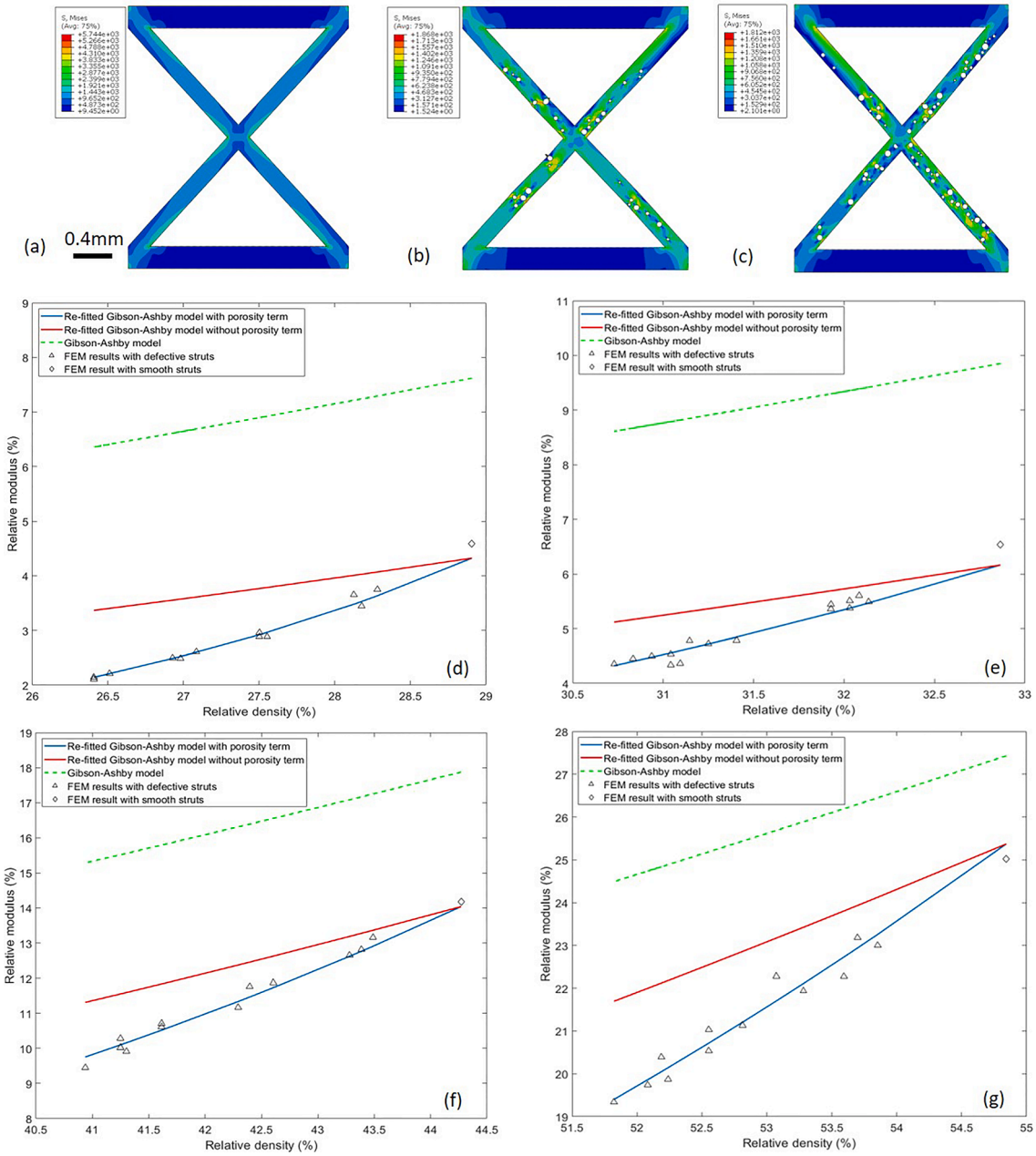

Fig. 4. Stress field of lattice with strut thickness of 0.4 mm and porosity of: (a) $\alpha = 0$, (b) $\alpha = 0.045$ and (c) $\alpha = 0.0965$ on the struts. Fitting for lattice structure with different porosity ranges from $\alpha = 0.0259 - 0.1957$, and with strut thickness of (d) 0.3 mm, (e) 0.4 mm, (f) 0.7 mm, and (g) 1 mm.

The integral constant C' naturally resolves to $C' = 1$. This is because in the absence of porosity defects in strut, i.e. $\alpha = 0$, the stiffness of the lattice should be equal to predictions obtained from GA model, viz. $\frac{E^*}{E_s} = C\left(\frac{\rho^*}{\rho_s}\right)^n$, i.e. $\beta = 1$ whereby $C' = 1$. This then suggests a more general form of GA model that incorporates the effect of porosity defects:

$$\frac{E^*}{E_s} = C\left(\frac{\rho^*}{\rho_s}\right)^n e^{-\kappa\alpha} \tag{8}$$

Results of this analyses are shown in Fig. 4d–g on the respective blue curves that show good fit, e.g., $R^2 > 0.93$ with numerically simulated values. Here, fit parameters were found to be $\kappa = 2.215, 1.288, 1.226,$

Table 2
Fitted Coefficients for Modified Gibson-Ashby Law that Incorporates Effects of Uniformly Distributed Porosity Defects.

Set #	Strut type	t_{strut} (mm)	α	C	n	κ	R^2
1	Smooth struts	0.1–1.0	/	1.334	2.763	/	0.9997
2	Porous struts- uniform	0.3	0.0511–0.1957	1.334	2.763	2.215	0.9826
3	Porous struts- uniform	0.4	0.0482–0.1125	1.334	2.763	1.288	0.9376
4	Porous struts- uniform	0.7	0.0283–0.1208	1.334	2.763	1.226	0.9737
5	Porous struts- uniform	1	0.0259–0.0791	1.334	2.763	1.412	0.9438

1.412, for $t_{strut} = 0.3\ mm,\ 0.4\ mm,\ 0.7\ mm,\ 1\ mm$, respectively. These are listed in Table 2. The mechanistic underpinnings of discrepancies in the parameter κ with respect to strut thickness of their parent lattices t_{strut} are pursued here via principal component analysis. Towards this, strain fields $\epsilon_{11}, \epsilon_{12}, \epsilon_{22}$ were extracted from central sections of struts featuring spatially uniform defect distributions, e.g., rows 1–5 in Table 1 and converted to their Fourier space amplitudes as described in Section 2.2. This was done separately for left leaning and right leaning struts, and results of these analyses are shown in Fig. 5. It is seen that PC1 readily distinguishes between ϵ_{11}, and ϵ_{22} strain fields obtained from lattices with defect-free struts as clearly observable separations in their respective projections with this component. Herein, ϵ_{11} strain fields of defect-free lattices with larger strut thickness, e.g. $t_{strut} = 1\ mm$, expressed comparatively smaller projections on the first principal

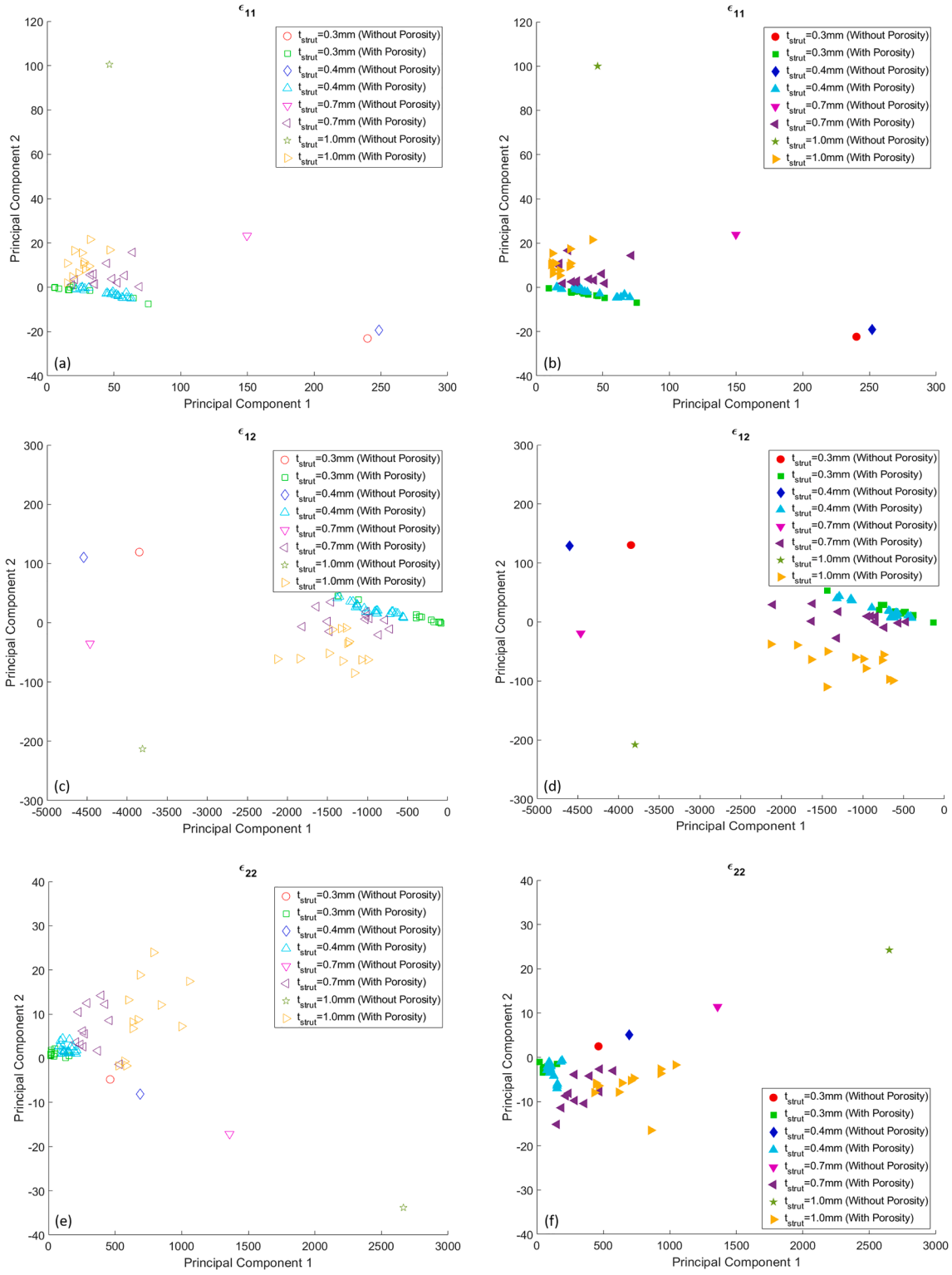

Fig. 5. PCA of elastic strain ϵ_{11} from: (a) right leaning strut, and, (b) left leaning strut, ϵ_{12} from (c) right leaning strut, and, (d) left leaning strut, and ϵ_{22} from (e) right leaning strut, and, (f) left leaning strut.

component axis as opposed to those obtained from thinner struts, e.g. $t_{strut} = 0.3$ *mm*, that exhibited larger projections. An opposite effect was seen for strain field ϵ_{22}, where defect-free lattices with smaller strut thickness, e.g. $t_{strut} = 0.3$ *mm*, expressed comparatively smaller projections on the first principal component axis, and larger struts, e.g., $t_{strut} = 1$ *mm* expressed comparatively larger projections. Separation was also seen in analogous PCA of ϵ_{12} strain field components, albeit one that could not be distinguished monotonically with respect to its projections on first or second principal component. Strain fields obtained from lattice structures with defective porous struts exhibited key deviations with respect to their defect-free counterparts. The separation between their projections and their corresponding defect-free analogues was obvious. However, the defective lattice structures were found to be clustered closer together in the space spanned by the first and second principal axes. Further, the defective lattice structures exhibited an anticipated spread corresponding to various defect configurations tested here. Within this cluster though, the defective lattice structures were found to be subtly separated from each other. It is noteworthy that these patterns are similar across left leaning and right leaning struts despite obvious differences between their defect configurations. These discrepancies are rationalized on the basis of the influence of free surfaces where traction vectors must resolve to $\underset{\sim}{n}.\underset{\sim}{\sigma} = \underset{\sim}{0}$ for maintaining local force equilibrium. Herein, lattice structures with porosity defects comprise significant free surface area, e.g., that existing in their inner walls, which can sufficiently distort the strain fields and leave a signature on their autocorrelation functions. These phenomena are expected to be magnified in lattices featuring smallest strut thicknesses or largest surface to volume ratios which is expected to translate to larger values of κ (Ref. Eq. (6)) in these structures. This is also seen from our examination of numerical results, e.g., $\kappa_{0.3\ mm} = 2.215 > \kappa_{0.4\ mm}(= 1.288), \kappa_{0.7\ mm}(= 1.226), \kappa_{1\ mm}(= 1.412)$.

From the arguments in the previous paragraph, it can be inferred that the mechanical behavior of the lattice structures that feature porosity defects is affected not just by the porosity fraction α, but also by the location of the defects. This conjecture is based on evidence presented in Fig. 4a that shows the von-Mises stress field in a perfect unit cell that is subject to elastic compressive deformation. Due to the bending dominated nature of this lattice, the struts exhibit larger von-Mises stresses close to their surfaces. Herein, the presence of a high density of porosity defects in such locations can alter the relative elastic response as well as the general mechanical response [25–30] of the parent strut, in comparison with what an equivalent density of uniformly distributed defects such as that shown in Figs. 4b, c would manifest. We note that an ensemble of such instances that feature high densities of defects close to the surface presents an additional source of variability in our model given in Eq. (8) that was calibrated using instances that featured uniformly distributed defects. To quantify this variability, we formulate a Bayesian inferencing framework that can model the response exhibited by our simulated instances probabilistically. Bayesian inferencing involves the use of the Bayes' theorem to estimate the distribution $P(H|E_1, \ldots, E_n)$ of a model parameter, e.g., H, given a certain number of simulated or empirically characterized data points, e.g., $E_1, \ldots, E_n$. This is formulated as:

$$P(H|E_1, \ldots, E_n) = \frac{P(E_1, \ldots, E_n|H)P(H)}{P(E_1, \ldots, E_n)} \tag{9}$$

, where $P(H)$ is the prior probability mass or density function of the model parameter H, $P(E_1, \ldots, E_n|H)$ is the probability of observing the data points $E_1, \ldots, E_n$, given the model parameter is H, and $P(E_1, \ldots, E_n)$ is the probability of observing data points $E_1, \ldots, E_n$, i.e.

$P(E_1, \ldots, E_n) = \int_{\Omega} P(E_1, \ldots, E_n|H)\, dG(H)$, where Ω is the domain of H, G being its cumulative distribution function. The term $P(E_1, \ldots, E_n|H)$ is also referred to as the likelihood $\mathscr{L}(H|E_1, \ldots, E_n)$. This formulation is iteratively implemented, wherein the posterior distribution of the previous iteration, i.e. $P(H|E_1, \ldots, E_{n-1})$ is used as the prior for the forthcoming iteration, i.e. $P(H)$ and updated as prescribed in Eq. (9) in light of newly available evidence E_n. By deploying a new data point in every iteration, the distribution of the model parameter H is iteratively updated till a pre-defined convergence criterion is met. The Bayesian inferencing methodology summarized in the previous paragraph was implemented for our datasets by setting the model parameter H as κ which is the random variable (RV) of interest (Ref. Eq. (8)). Based on this parameterization the observations referred to as E_i in Eq. (9), where $i \in \{1, \ldots, n\}$, correspond to the RV E_{GA}- the predicted relative elastic modulus, which is a function of RVs κ, and porosity fraction α (Ref. Eq. (8)). This enables us to formulate the likelihood function as Gaussian, i.e., $\mathscr{L}(\kappa|E_{GA}) = P(E_{GA} = E_{FEM}|\kappa) \propto \exp\left(-\frac{(E_{GA}-E_{FEM})^2}{2h^2}\right)$. Here, $\frac{E_{GA}}{E_s} = C\left(\frac{\rho^*}{\rho_s}\right)^n e^{-\kappa\alpha}$, and $h = 1.06\sigma q^{-1/5}$ is the standard error given standard deviation of observed data σ, and the number of samples q [31,32]. With this notion, the Bayesian inferencing framework that attempts to encapsulate the behavior of our material system comprising defective lattice structures is given by:

$$P(\kappa|E_{GA} = E_{FEM}) = \frac{P(E_{GA} = E_{FEM}|\kappa)P(\kappa)}{P(E_{GA} = E_{FEM})} \tag{10}$$

The first step towards the numerical implementation of this framework involved calibration with respect to specimens in which porosity defects were uniformly distributed. This was done individually for the 4 different strut thicknesses of the BCC lattice studied in the present work. Herein, a non-informative prior, i.e. uniform distribution was assigned to the RV κ in each of these cases. These distributions were centered about their nominally observed values given in Table 2, i.e. $\kappa \in (1.715, 2.715), (0.788, 1.788), (0.726, 1.726), (0.912, 1.912)$, for $t_{strut} = 0.3$ *mm*, 0.4 *mm*, 0.7 *mm*, 1 *mm*, respectively. These prior distributions were multiplied with respective Likelihood functions $\mathscr{L}(\kappa|E_{GA})$ in an elementwise manner and the result was normalized, thus providing the posterior distribution, e.g. LHS in Eq. (10). The values of the parameter α that were used for constructing these likelihood functions are shown in Figs. 4d–g for $t_{strut} = 0.3\ mm, 0.4\ mm, 0.7\ mm, 1\ mm$, respectively. The aforementioned posterior distribution served as prior distributions for their next iterations, respectively. In every step, the most likely point estimate of the RV κ was extracted from the corresponding posterior distribution. Using this estimate, the goodness of fit of the model in Eq. (8) was calculated with respect to the simulated behavior of all numerical specimens that featured the same strut thickness and comprised a uniform distribution of defects. The iterations were terminated after 12–15 steps. In each case, a goodness of fit $R^2 > 0.93$ was obtained at the end of these iterations. Fig. 6 shows the implementation of our Bayesian inferencing model as applied to lattice structures with uniformly distributed porosity defects. Starting with a uniform prior distribution, this approach was able to provide a most likely point estimate of parameter κ at the end of iterations that closely matched its nominal counterparts, e.g., those obtained using least square error based regression. For instance, the probabilistically inferred values of this parameter were $\kappa = 2.210,\ 1.280,\ 1.217,\ 1.412$, compared with nominal values, which were $\kappa = 2.215,\ 1.288,\ 1.226,\ 1.412$, for $t_{strut} = 0.3\ mm$, 0.4 *mm*, 0.7 *mm*, 1 *mm*, respectively. Herein, an important pattern in the convergence of the posterior distributions of κ for different values of t_{strut} is immediately obvious, that a larger number of simulated observations produces a point estimate of κ that matches the nominally produced counterpart with greater probability. A conservatively large number, e.g., > 500, of simulations was not pursued in the present work that would allow the estimation of the standard deviation of κ from its inferred distribution. Nonetheless, we still report the variability in the simulated behavior of defective lattice structures as the standard deviation of the posterior distribution of κ that is inferred after 12–15 iterations, viz. $\sigma \sim 0.24,\ 0.18,\ 0.22,\ 0.13$. This suggests an inferred effective variability of $\frac{\sigma}{\kappa} \sim 0.11,\ 0.14,\ 0.18,\ 0.13$, for $t_{strut} = 0.3\ mm$, 0.4 *mm*, 0.7 *mm*, 1 *mm*, respectively. A 20% change in parameter κ, e.g.,

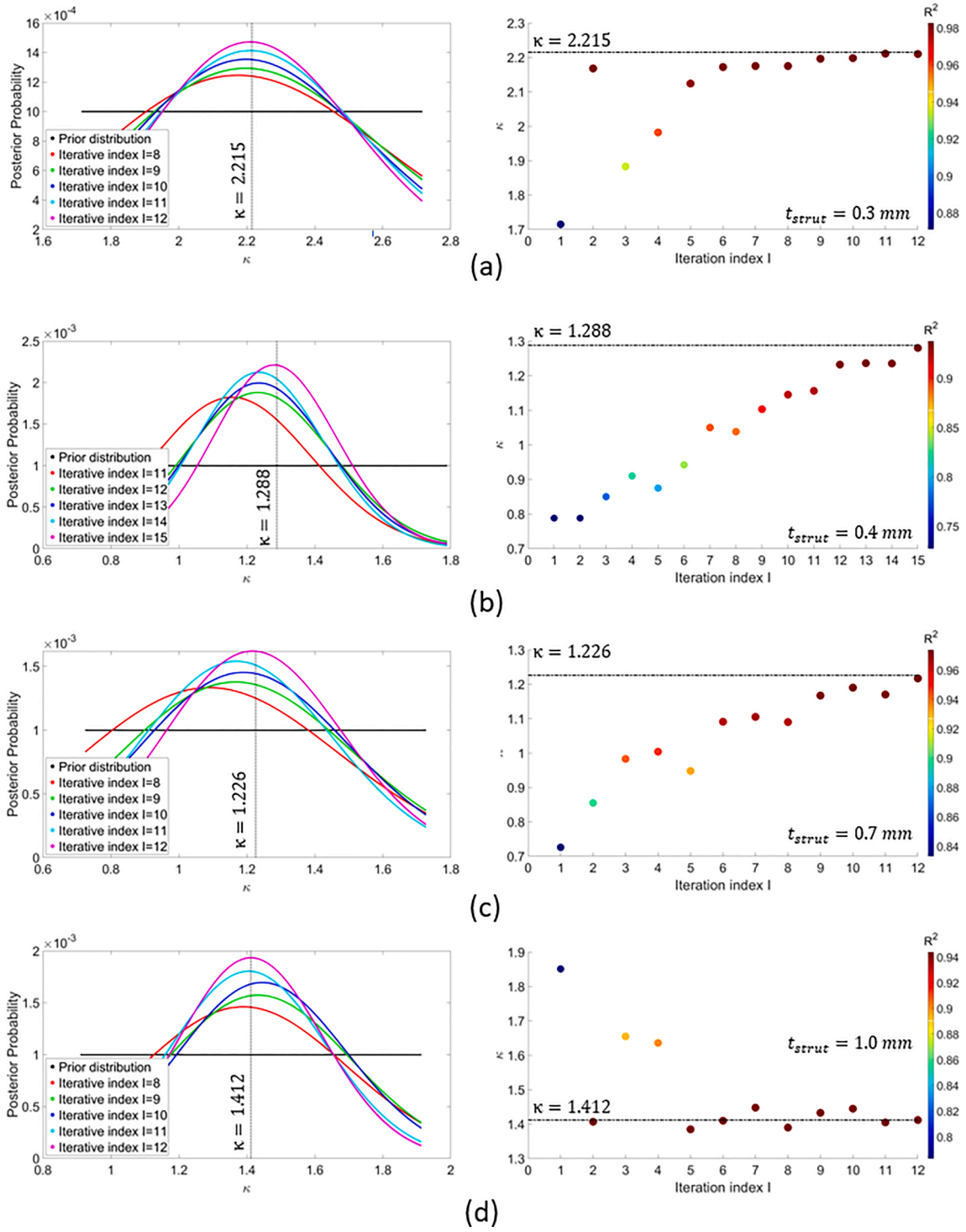

Fig. 6. Variability analysis for lattice structures featuring uniformly distributed defects. Strut thicknesses t_{strut} in the figures correspond to: (a) 0.3 mm, (b) 0.4 mm, (c) 0.7 mm, (d) 1 mm. The subfigures on the left hand side show the inferred distribution of parameter κ in the last 5 iterations. The horizontal line shows the uniform prior distribution. The vertical line corresponds to the nominal value of κ given in Table 2. The subfigures on the right hand side show goodness of fits R^2 of the most likely point estimates of parameter κ inferred and their convergence to the nominal κ shown using horizontal line, at various stages o.f the iteration.

for $t_{strut} = 0.7\ mm$ albeit likely in one instance of a lattice structure with probability $P(\kappa > \mu_{t_{strut}=0.7\ mm} + \sigma) \sim 0.45$ rapidly decays to background noise levels, e.g. $P(\cap_{i=1}^{6} \kappa_i > \mu_{t_{strut}=0.7\ mm} + \sigma) = \Pi_{i=1}^{6} P(\kappa_i > \mu_{t_{strut}=0.7\ mm} + \sigma) = 0.45^6 \sim 8 \times 10^{-3}$. In this regard, such an occurrence is highly unlikely until it is driven by a fundamental change in the behavior of the parent lattice structure such as a reduction in its thickness or change in its geometry. Such a change may also be instigated by an input change in the spatial arrangement of the defects. To test the influence of the spatial arrangement of defects on mechanical response, lattice structures with high density of defects close to surfaces were generated numerically. Defect densities within a similar range as shown in Fig. 4d–g were used. Herein, the spatial location of these defects was confined within a band of thickness $0.2t_{strut}$ in the vicinity of the respective surface. Note, this arrangement of defects enables us to make comparisons between such lattice structures and their counterparts of equal strut thickness t_{strut}, but

which comprise spatially uniform defect distributions. Such comparison would be complicated if defects were strictly confined within a band of absolute specified thickness, wherein the fractional thickness of this band, e.g., ft_{strut}, would be different across every structure studied here. Towards this end, the fraction $f = 0.2$ was arbitrarily chosen. The objective of the present research is to formulate a framework that can delineate the changes to mechanical response resulting from probabilistic changes to spatial distributions of defects. We show in the forthcoming paragraphs that we are able to achieve this objective. Nonetheless, the authors intend to extend this research to understand the influence of different fractional band thicknesses in the future. The mechanical response of lattice structures with high density of defects close to the surface was numerically simulated with a protocol that mirrored the one used for their spatially uniform counterparts (cf. Section 2.1). Subsequently, this simulated data was compiled using an approach discussed in Section 3.2. Lattices with surface defects exhibited nominal values of parameter κ that were moderately different for $t_{strut} = 0.3\ mm$, and considerably different for $t_{strut} = 0.4\ mm,\ 0.7\ mm,\ 1\ mm$, with respect to their spatially uniform counterparts. For instance, $\kappa = 2.134,\ 1.623,\ 1.016,\ 1.092$ for surface defects (summarized in Table 3), in comparison with $\kappa = 2.215,\ 1.288,\ 1.226,\ 1.412$ for spatially uniform defects. These correspond to relative differences of $\frac{|\Delta\kappa|}{\kappa_{uniform}} \sim 0.04,\ 0.26,\ 0.17,\ 0.23$ for $t_{strut} = 0.3\ mm,\ 0.4\ mm,\ 0.7\ mm,\ 1\ mm$, respectively. These values provided adequate goodness of fits $R^2 \sim 0.96,\ 0.97,\ 0.96,\ 0.94$, respectively, with respect to numerically simulated mechanical responses. However, a consistent pattern between parameter κ for surface and uniform defect distributions was not found suggesting a complex interaction between the defects and the surrounding stress field within the structure. This data was used to establish another Bayesian inferencing framework, with the objective of analyzing the resulting standard deviation of parameter κ. For this framework, a non-informative, e.g., uniform prior distribution wasalso used for parameter κ. Fig. 7 shows the results of this analysis, illustrating similar convergence characteristics with the spatially uniform counterparts. These characteristics include the general trend, that a larger number of observed data points resulted in most likely point estimates of κ that became progressively closer to their nominal counterparts with greater probability. At the end of 12–15 iterations, these most likely points estimates were $\kappa = 2.145,\ 1.623,\ 1.019,\ 1.097$, for $t_{strut} = 0.3\ mm, 0.4\ mm, 0.7\ mm, 1\ mm$, near identical to counterparts obtained via regression, i.e. $\kappa = 2.134,\ 1.623,\ 1.016,\ 1.092$, respectively. Standard deviations σ were extracted from the posterior distributions of parameter κ for structures featuring $t_{strut} = 0.3\ mm, 0.4\ mm,\ 0.7\ mm,\ 1\ mm$ and were found to be $\sigma \sim 0.22,\ 0.21,\ 0.2,\ 0.14$, respectively. These suggest effective variabilities of $\frac{\sigma}{\kappa} \sim 0.10,\ 0.17,\ 0.2,\ 0.13$, which were only marginally different than their spatially uniform counterparts that exhibited $\frac{\sigma}{\kappa} \sim 0.11,\ 0.14,\ 0.21,\ 0.14$, respectively.

It is clear from this analysis that the spatial distribution of defects can significantly alter the mechanical response of structures. In order to test the efficacy of a simplified, e.g. single parameter model (cf. Eq. (8)) at accounting for such variances, the Bayesian inferencing models illustrated in Figs. 6 and 7 were merged. For doing the same the posterior distributions of κ for various structures comprising uniform defects (e.g., distributions illustrated in magenta corresponding to last iteration in Fig. 6) were used as prior and updated with mechanical response of structures comprising high density of surface defects. The most likely point estimates of κ were extracted in each step and the goodness of fit of the model given in Eq. (8) was found with respect to all data sets, e.g., surface defects + uniform defects. This was done individually for structures featuring different strut thicknesses. Fig. 8 illustrates this framework. The most likely point estimates of κ predicted by the merged Bayesian framework were $\kappa = 2.171,\ 1.424,\ 1.101,\ 1.195$. These values provided only marginally different (sometimes exceeding) goodness of fits, e.g., $R^2 = 0.98,\ 0.94,\ 0.96,\ 0.91$, for $t_{strut} = 0.3\ mm, 0.4\ mm, 0.7\ mm, 1\ mm$, respectively. Given that an equal number of instances comprising spatially uniform defects, and surface defects were used for constructing this model, these κ values were also approximately midway between the inferred values of the respective struts, e.g., $\kappa = 2.210,\ 1.280,\ 1.217,\ 1.412$, for uniformly distributed defects (cf. Table 2), and $\kappa = 2.145,\ 1.623,\ 1.019,\ 1.097$, for surface defects, respectively (cf. Table 3). Interestingly, merging of the two datasets within this Bayesian framework resulted in smaller standard deviations after all iterations were complete, e.g., $\sigma \sim 0.18,\ 0.14,\ 0.16,\ 0.12$, when compared with standard deviations of distributions inferred from instances comprising surface, or uniform defects alone. This is a promising result that testifies to the efficacy of a single parameter model such as Eq. (8) in encapsulating different modalities of spatial defect distributions. However, the framework is based on an implicit assumption, that the mechanical response of structures comprising a high density of defects near the surface is not dramatically different than those comprising a spatially uniform distribution of defects. Realistically, differences in spatial distribution of defects can arise in additively manufactured components if build parameters are appropriately changed. The manufacturing community has generally focused on reducing the density of defects uniformly throughout the volume, wherein a single modality of spatial defects is anticipated in real specimens. It is envisioned that the mechanics of such unique modalities can be well encapsulated by the model in Eq. (8).

3.3. The effect of roughness on mechanical response of lattice structures

Fig. 9a shows the numerically simulated influence of sinusoidal surface roughnesses on the mechanical response of lattice structures. With respect to the perfectly smooth counterpart, lattice structures with rougher surfaces exhibit degradation in their relative moduli $\frac{E^*}{E_s}$. It is seen from Fig. 9b that this degradation is highly dependent on the mechanics of the parent strut. For instance, a comparatively larger degradation caused by roughness was seen in lattice structures with thinner struts. This trend was quantified as the ratio of the relative moduli of rough, e.g. $\frac{t_{min}}{t_{max}} \sim 0.8$, and smooth struts, e.g., $\frac{t_{min}}{t_{max}} = 1$, as $\frac{E^*_{rough}}{E_s} / \frac{E^*_{smooth}}{E_s} \sim 0.94,\ 0.82,\ 0.95$for $t_{strut} = 0.7\ mm,\ 0.4\ mm, 0.3\ mm$, respectively. The source of this degradation was found to lie in the roughness peaks of these surfaces that cannot efficiently accommodate external deformation boundary conditions imposed on the lattice structure. This is evidenced in the rapid decay of stresses within them as shown in the inset in Fig. 9a. However, the GA model is incapable of modeling this effect because a sinusodal roughness despite producing a degradation in the mechanical response of lattice structure $\frac{E^*}{E_s}$ does not change its relative density $\frac{\rho^*}{\rho_s}$. This shortcoming can be addressed by following a similar line of thought as

Table 3
Fitted Coefficients for Modified Gibson-Ashby Law that Incorporates Effects of Surface Distributed Porosity.

Set #	Strut type	t_{strut} (mm)	α	C	n	κ	R^2
1	Smooth struts	0.1–1.0	/	1.334	2.763	/	0.9997
6	Porous struts- surface	0.3	0.0340–0.1957	1.334	2.763	2.134	0.9608
7	Porous struts- surface	0.4	0.0289–0.1286	1.334	2.763	1.623	0.9701
8	Porous struts- surface	0.7	0.0264–0.1075	1.334	2.763	1.016	0.9629
9	Porous struts- surface	1	0.0314–0.0791	1.334	2.763	1.092	0.9393

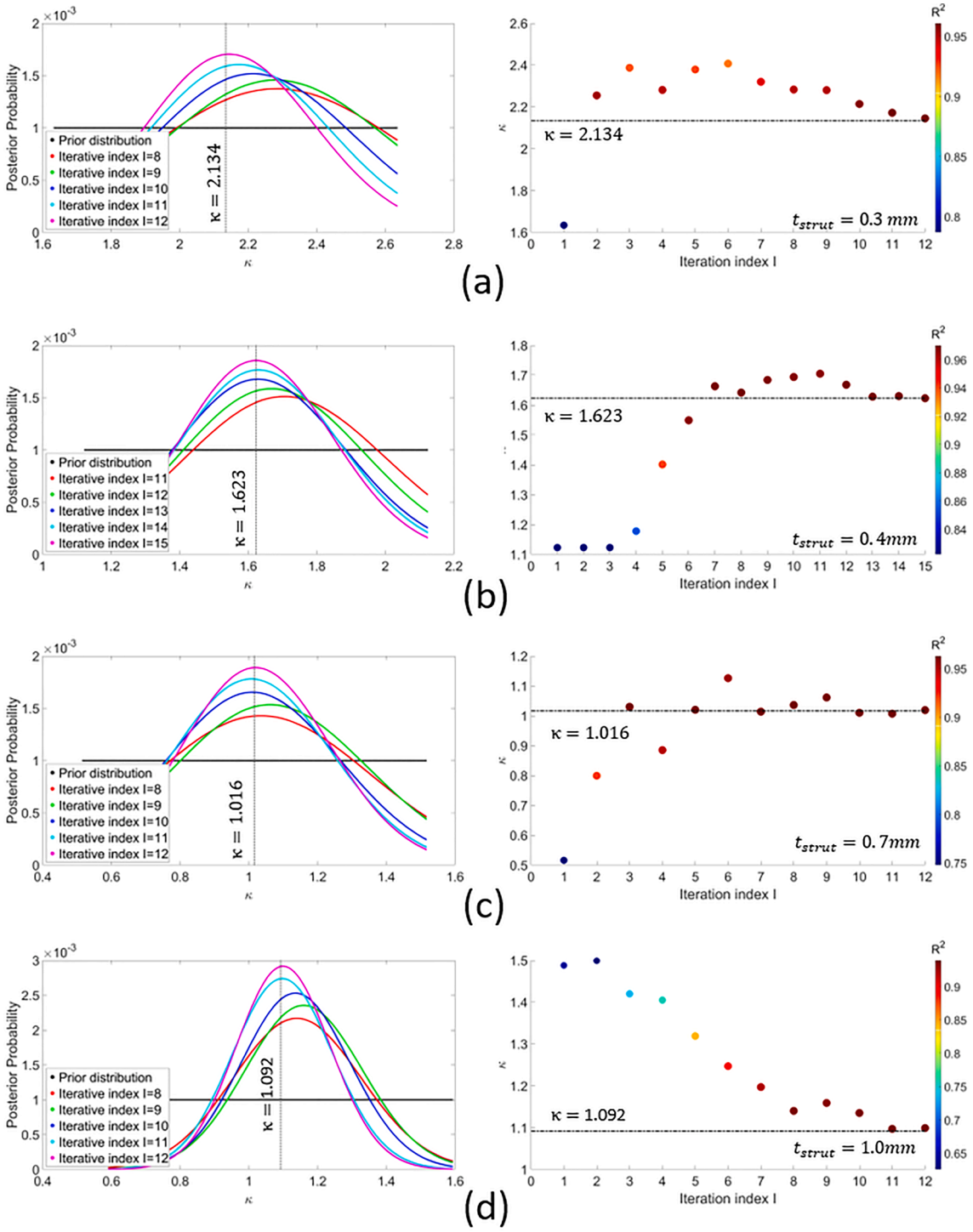

Fig. 7. Variability analysis for lattice structures featuring surface defects. Strut thicknesses t_{strut} in the figures correspond to: (a) 0.3 mm, (b) 0.4 mm, (c) 0.7 mm, (d) 1 mm. The subfigures on the left hand side show the inferred distribution of parameter κ in the last 5 iterations. The horizontal line shows the uniform prior distribution. The vertical line corresponds to the nominal value of κ given in Table 3. The subfigures on the right hand side show goodness of fits R^2 of the most likely point estimates of parameter κ inferred and their convergence to the nominal κ shown using horizontal line, at various stages o.f the iteration.

given in Section 3.2 where it was assumed that degradation to the mechanical response of lattice structures takes place in relation to their current state (Ref. Eq. (6)). This hypothesis results in the equation:

$$\frac{E^*}{E_s} = C\left(\frac{\rho^*}{\rho_s}\right)^n k_{r_1} e^{k_{r_2}\frac{t_{min}}{t_{max}}} \tag{11}$$

Here, $\frac{t_{min}}{t_{max}} \approx 1 - \frac{4a}{t_{strut}}$ (e.g., when $\frac{a}{t_{strut}} \ll 1$), is a measure of the surface roughness. This formulation suggests that for a smooth surface, i.e. $\frac{t_{min}}{t_{max}} = 1, \frac{E^*}{E_s} = C\left(\frac{\rho^*}{\rho_s}\right)^n$, implying $k_{r_1} = e^{-k_{r_2}}$. Fig. 9b shows the comparison of the original GA model with this roughness effect term for nominal strut thickness $t_{strut} = 0.3\ mm, 0.4\ mm, 0.7\ mm$ and roughness metric $\frac{t_{min}}{t_{max}}$ ranging between $0.5789-0.9868$, $0.6667-0.9900$, $0.7949-0.9943$, respectively. The fitting coefficient for these lattices were found to be $(kr1,\ kr2) = (0.9574,\ 0.1091)$, $(0.5881,\ 0.612)$, $(0.7282,\ 0.3341)$, respectively. It is noteworthy that here, $kr1 \approx e^{-kr2}$, e.g. $kr1 \times$

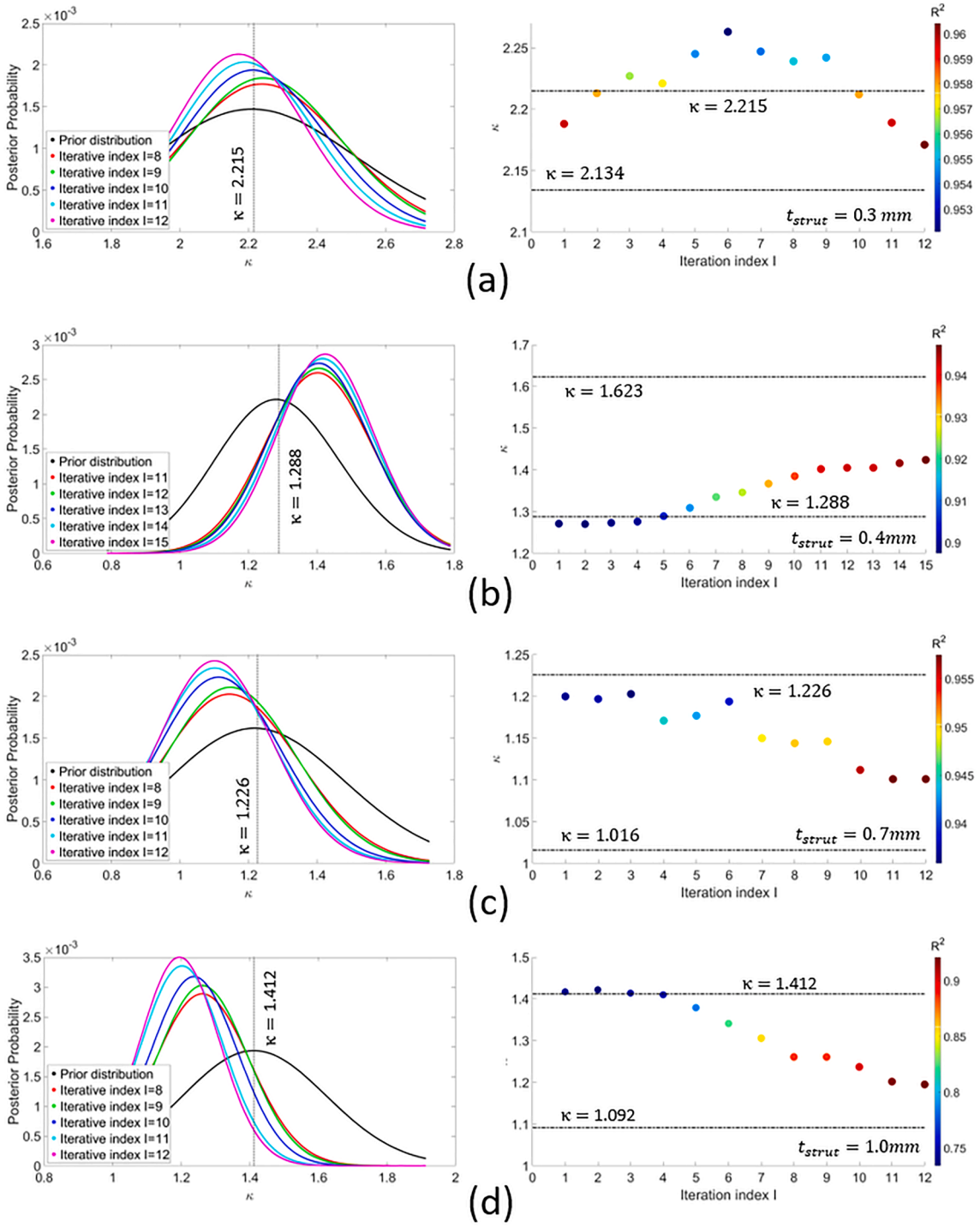

Fig. 8. Variability analysis for lattice structures featuring uniform and surface defects. Strut thicknesses t_{strut} in the figures correspond to: (a) 0.3 mm, (b) 0.4 mm, (c) 0.7 mm, (d) 1 mm. The subfigures on the left hand side show the inferred distribution of parameter κ in the last 5 iterations. The vertical line corresponds to the nominal value of κ that is obtained from the instances featuring spatially uniform distribution of defects. The subfigures on the right hand side show goodness of fits R^2 of the most likely point estimates of parameter κ inferred. The horizontal lines show nominal values of κ for uniform and surface defects.

$e^{kr2} \sim 1.07, 1.08, 1.02$, respectively. This fitting coefficients produced coefficient of determinations $R^2 > 0.93$, as listed in Table 4.

The salient aspects of strain fields expressed by lattice structures with rough struts were studied via PCA. This is shown in Fig. 10 for left and right leaning struts separately. Towards this, the protocol described in Section 2.2 was followed. Here, strain fields obtained from struts featuring thicknesses $t_{strut} = 0.3\ mm, 0.4\ mm$, and $0.7\ mm$ and roughness parameters $\frac{t_{min}}{t_{max}} = 0.5789 - 0.9868, 0.6667 - 0.9900, 0.7949 - 0.9943$ were used respectively. Note, porosity defects were ignored in this analysis. Due to this reason, a completely new set of principal axes can be generated, wherein the location of even defect-free struts, e.g. those featuring $\frac{t_{min}}{t_{max}} = 1$ can be expected to be completely different than their analogous positions that the PCA using lattice structures with porosity defects would predict. Indeed, this was the case as seen in Fig. 10 where the projections of Fourier representations of autocorrelations of strain fields expressed values that did not match their aforementioned

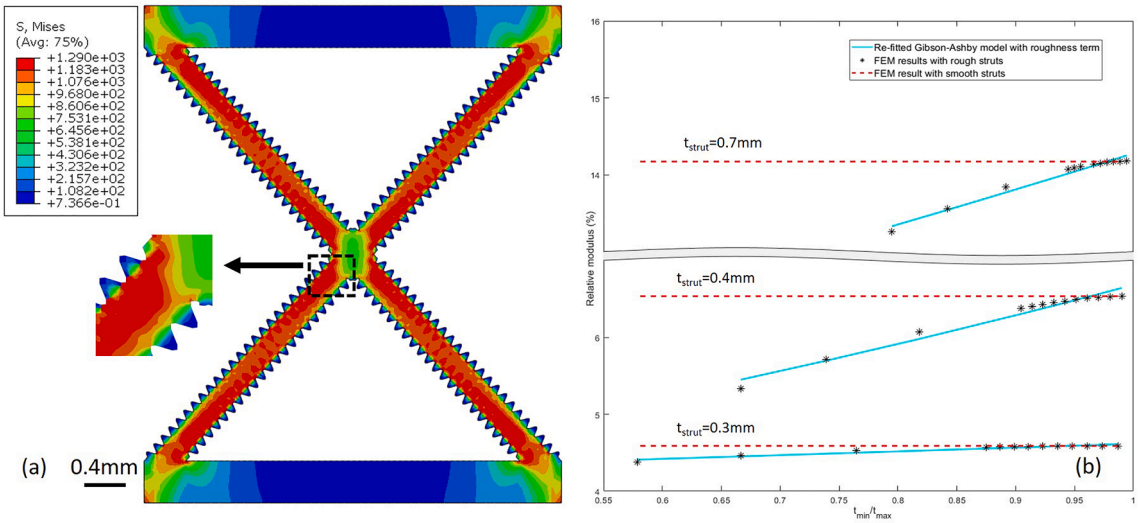

Fig. 9. (a) Stress field of lattice structure with surface roughness, featuring $\lambda = 0.108$ mm, a = 0.016 mm and $t_{strut} = 0.4\,mm$. (b) Fitting for lattice structure with $t_{strut} = 0.4\,mm$ and different roughness on struts.

Table 4
Fitted Coefficients for Modified Gibson-Ashby Law that Incorporates Effects of Surface Roughness.

Set #	Strut type	t_{strut} (mm)	t_{min}/t_{max}	C	n	k_{r1}	k_{r2}	R^2
1	Smooth struts	0.1–1.0	1	1.334	2.763	/	/	0.9997
10	Rough struts	0.3	0.5789–0.9868	1.334	2.763	0.9574	0.1091	0.9326
11	Rough struts	0.4	0.6667–0.9900	1.334	2.763	0.5881	0.612	0.9665
12	Rough struts	0.7	0.7949–0.9943	1.334	2.763	0.7282	0.3341	0.9720

counterparts seen in Fig. 5. Nonetheless, even this new set of principal axes were able to separate lattice structures featuring different nominal strut thicknesses $t_{strut} = 0.3\ mm, 0.4\ mm$ and $0.7\ mm$. Further, their projection values along the first principal component also showed monotonic increase with respect to the parameter t_{strut}.

The projections of auto-correlations of strain fields in their Fourier representations that were obtained from lattice structures with rough struts expressed interesting variations that were not exhibited by their smooth counterparts. Herein, the strut with the smallest thickness used for this analyses, e.g. $t_{strut} = 0.3mm$ exhibited little separation between their smooth and rough counterparts on the space spanned by the first 2 principal axes.This separation was however more dominant, albeit similar in lattice structures with thicker struts $t_{strut} = 0.4\ mm$ and $0.7\ mm$. Further, unlike strain fields expressed by lattice structures with porous struts, those resulting from rough struts generally did not 'cluster' in the vicinity of each other, but neatly arrange linearly in this space spanned by the first two principal axes. This is most obvious for strain fields obtained from lattice structure featuring $t_{strut} = 0.4\ mm$. The reason behind this observation is that in comparison with the randomness of porosity defects that manifested the random clustering of projections seen in Fig. 5, strain fields here were influenced by periodic sine waves that obviously lack this randomness. This lack of randomness produces more regular projections as seen in Fig. 10. Herein, the lattice structure with the thickest strut $t_{strut} = 0.7\ mm$ studied for this analyses exhibited variations in their projections on the principal axes that were also highly correlated to their surface roughness measure, viz. $\frac{t_{strut}-2a}{t_{strut}+2a}$ as shown in Fig. 10.

3.4. The combined influence of porosity and surface roughness defects on mechanical response

Insights obtained so far in Section 3 can enable formulation of predictive models of the mechanical response of complex lattice structures. Towards the same, it is realized that typical lattice structures possess a combination of porosity and surface roughness defects. In this regard, a more complex and more compromised response can be expected in a typical lattice structure. This was analyzed by simulating the response of 1×1 dimensional structures with struts featuring $t_{strut} = 0.4\ mm$. Herein, two different roughness measures were tested featuring sine amplitudes $a = 0.004\ mm,\ 0.016\ mm$, corresponding to $R_a = 2.5\ \mu m$, $10.2\ \mu m$, respectively. Both surface roughnesses were generated with the same wavelength that was used to calibrate the model described in Section 3, viz. $\lambda = 108\ \mu m$. Porosity fractions similar to those used for calibration were assigned to these lattice structures, whereby relative densities $\frac{\rho^*}{\rho_s}$ between 30% −32.5% were analyzed. The macroscopic behavior of these structures was modeled as:

$$\frac{E^*}{E_s} = C\left(\frac{\rho^*}{\rho_s}\right)^n e^{-\kappa\alpha}\ k_{r_1} e^{k_{r_2}\frac{t_{min}}{t_{max}}} \tag{12}$$

This form multiplicatively combines the effects of porosity and roughness within the same response equation. Note, constraints on the respective porosity and roughness terms, viz. $e^{-\kappa\alpha}, k_{r_1} e^{k_{r_2}\frac{t_{min}}{t_{max}}}$, respectively, ensure that Eq. (12) collapses to Eq. (11), Eq. (8), or simply the Eq. (1), in the absence of porosity, or roughness defects, or in a pefect defect-free state, respectively. Herein, such a multiplicative combination also implicitly assumes that roughness or porosity defects do not affect the fundamental influence of each in the presence of the other.

Figs. 11 shows results of two instances of lattice structures pertaining to roughness values $R_a = 2.5\ \mu m, R_a = 10.2 \mu m$, and porosity fractions $\alpha = 0.0386,\ 0.0482$, respectively. Stress fields in these lattice structures simultaneously shared characteristics with those that exclusively featured porosity, and surface roughness defects (cf. Sections 3.2, 3.3, respectively). These characteristics include stress concentrations in the vicinity of porosity defects, like in Fig. 4, and decaying stress fields within roughness peaks, like in Fig. 9. Figs. 11b, d show the mechanical response of such lattice structures featuring a combined influence of

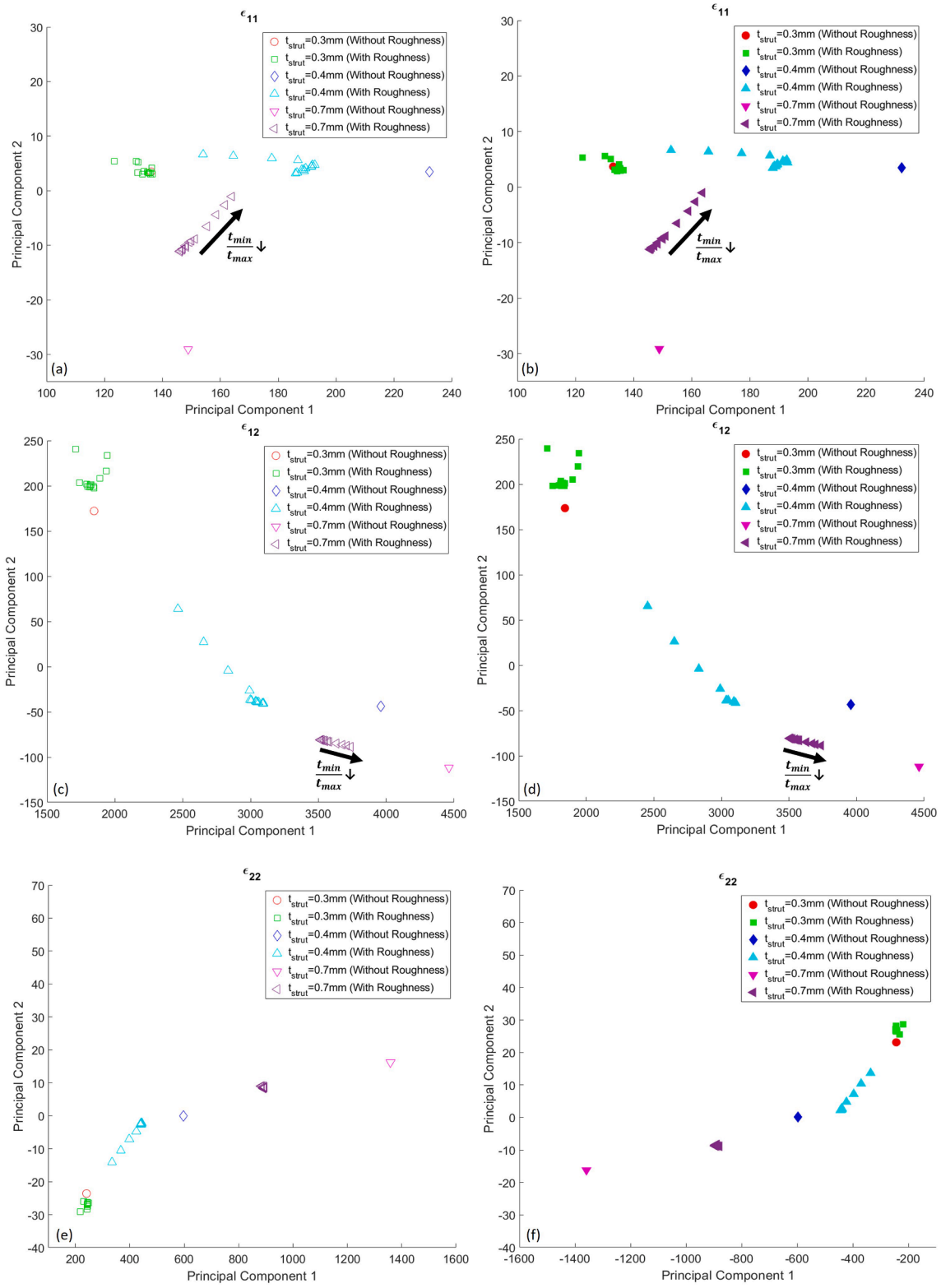

Fig. 10. PCA for elastic strain from rough struts. Hollow markers on the left column represent strains extracted from left leaning struts, e.g.,top-left to bottom-right, while solid marker on the right columns represent strains extracted from the right leaning struts.

porosity and surface roughness (cf. hollow triangles). For comparison, the response predicted by the original GA form, e.g., Eq. (1) that is calibrated for 3D BCC structures, and that calibrated for our 2.5D plane stress BCC structures is also shown in this figure using green, and red curves, respectively. Towards delineation the influences of roughness and porosity, fitting coefficients gathered from controlled studies described in Sections 3.2, and 3.3 were initially used here, viz. $(C,n,\kappa,k_{r1},k_{r2}) = (1.334, 2.763, 1.288, 0.5881, 0.612)$. These fitting coefficients were able to characterize the response $\frac{E^*}{E_s}$ of lattice structures within 15% of the values that were predicted numerically. It is noteworthy that this model, based on multiplicative coupling of porosity and surface

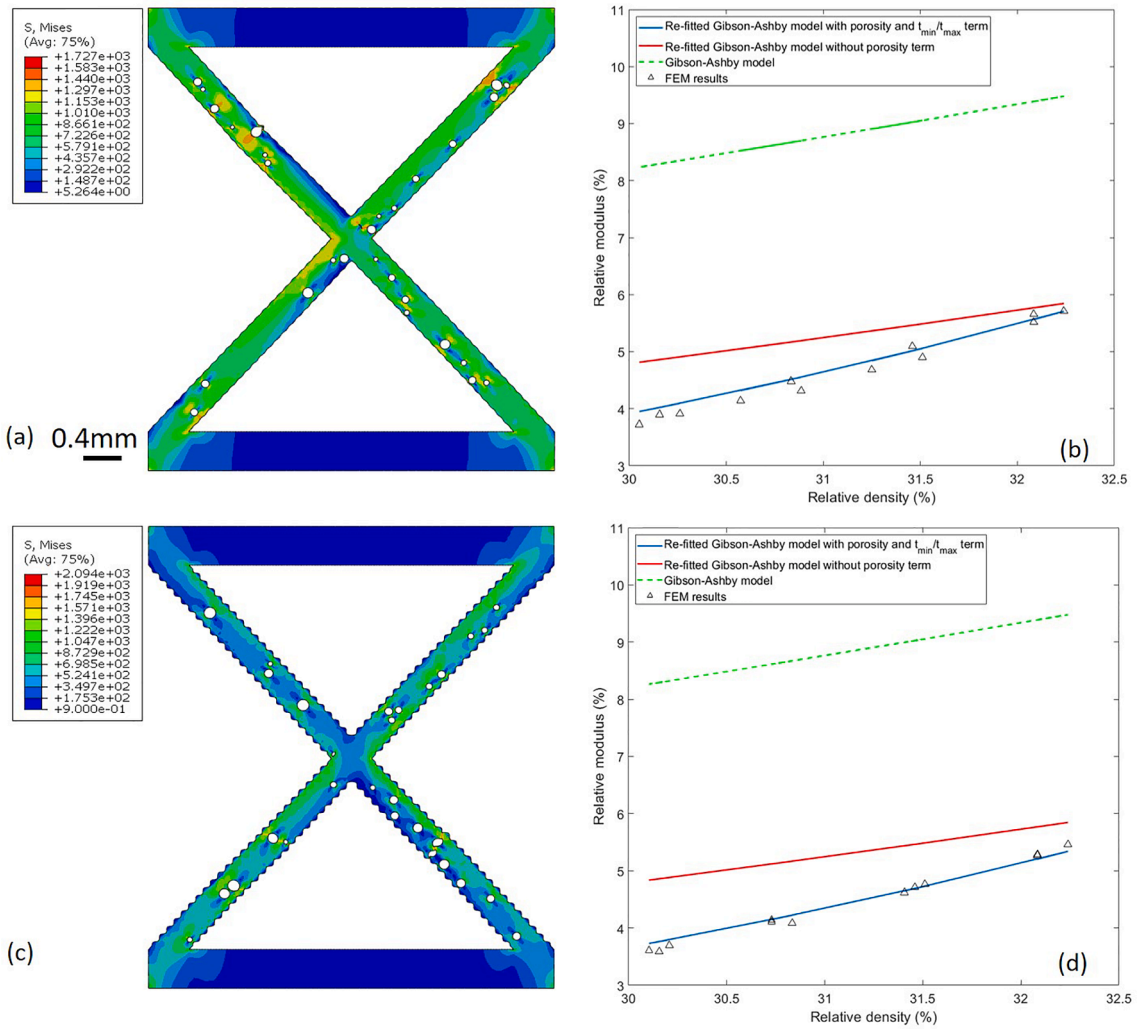

Fig. 11. Stress field of lattice structure with $\lambda = 0.108$ mm, (a) a = 0.004 mm and $\alpha = 0.386$, and (c) a = 0.016 mm and $\alpha = 0.0482$. (b, d) The mechanical response of lattice structures with strut dimension corresponding to (a, c), at various relative densities $\frac{\rho^*(\alpha)}{\rho_s}$.

roughness defects slightly overestimated the response compared with that predicted by numerical simulations. This suggests an interaction between these defects, which further degrades their relative elastic moduli, e.g., when both defects are present. In the present work, this discrepancy could be resolved by adjusting the value of k_{r1} to 0.57. This relatively minor change produced coefficient of determination of $R^2 > 0.95$ in both these cases, as listed in Table 5.

3.5. Implications of this work

The simulation framework described in this paper was used to demonstrate how porosity defects and topography defects introduced by metal AM processing degrades the relative stiffness of a printed lattice. However, the complexity and significance of these defects in practice have been understated thus far. So are the challenges of correcting them. The reasons are as follows.

- Stiffness is an extremely important performance measure for a lattice, but fatigue resistance is equally if not more important. Furthermore, it is believed to be far more sensitive to defects.
- Metal AM processes do not leave behind porosity defects that are uniformly distributed throughout the bulk. Instead, a higher concentration are typically observed near the surface, many of these are surface interconnected. As such, they are incapable of being healed by HIP. Furthermore, under high temperature conditions, bulk porosity defects healed by HIP often reappear to varying degree.
- The surface topography created by metal AM processes is heavily influenced by staircasing and partial powder solidification. In turn, these factors are extremely sensitive to surface orientation relative to the build direction. Consequently, metal AM parts typically have surfaces with extremely heterogenous topography.
- Simple quantitative measures of surface topography such as R_a are not necessarily good metrics to target, because it is possible for a

Table 5
Fitted Coefficients for Modified Gibson-Ashby Law that Incorporates Effects of Uniform Porosity and Surface Roughness.

Set #	Strut type	t_{strut} (mm)	α	t_{min}/t_{max}	C	n	κ	k_{r1}	k_{r2}	R^2
1	Smooth struts	0.1–1.0	/	/	1.334	2.763	/	/	/	0.9997
13	Rough, porous	0.4	0.048–0.161	0.961	1.334	2.763	1.288	0.57	0.612	0.9536
14	Rough, porous	0.4	0.048–0.167	0.923	1.334	2.763	1.288	0.57	0.612	0.9792

surface riddled with surface interconnected porosity defects to have the same R_a value as one that does not. Consequently, while a surface may appear to be fatigue resistant on account of its perceived smoothness, it may not be.

- An objective of the metal AM community is to print ever thinner lattices. However, the invariable increase in defect concentration is going to be a limiting factor. In response, AM processing technology will continue to advance so that lower defect concentrations may be realized. However, this will invariably require greater process lead time or greater process cost to achieve.
- A super finishing process cannot be used to directly control geometry. It is a material erosion process, that if carried out in a repeatable manner, leads to consistent localized material removal and consistent localized surface topography. However, process development requires multiple iterations of trial, measurement, part redesign, and process redesign to derive feasible solutions.
- Super finishing processes remove material from surface topographies in different ways, causing the geometries of the peaks, valley, and surface interconnected defects to evolve in different ways. The rate at which they remove material is process dependent as well.
- The localized removal rate of super finishing processes is relatively low. But they are capable of completely machining through skin into the bulk volume with sufficient processing time. Consequently, they are capable of not only removing surface defects but sub surface defects as well.

In summary, defect management is critical to the performance and cost of printed parts, especially those that are light weighted with latticing or topology optimization. With continued development, the simulation framework presented in this work can become a powerful tool to explore how defect distribution and geometry affect lattice stiffness, buckling, and stress concentrations. Knowledge of this will allow the design and processing community to make better engineering decisions.

4. Conclusions and future work

1. The present work demonstrates the effect of volumetric porosity and surface roughness defects on the elastic response of 2.5 D BCC lattice structures. Implementation of this workflow involved the python interface of Abaqus that was used to generate these structures and implant them with circular porosity and sinusoidal surface roughness defects. Subsequently their elastic response was numerically simulated, whereby their relative elastic moduli were characterized.
2. It was seen that the influence of porosity defects and surface roughnesses can be modeled as exponential degradations to the response of the defect-free lattices. Herein, fitting coefficients of these exponential degradation terms were found to be influenced by the parameters of the parent structure itself. Lattices with thinner struts generally exhibited more rapid degradations in response to increasing densities of porosity defects and larger surface roughnesses.
3. A Bayesian inferencing framework was formulated to delineate the effect of changes in spatial distribution of porosity defects on the mechanical response of the parent structures. It was seen that different modalities of these distributions can profoundly affect the mechanical response. The Bayesian inferencing model was trained using an equal number of simulated instances of both types of structures, e.g., those comprising uniformly distributed, and surface porosities, for various strut thicknesses t_{strut} studied here. This model was able to predict a most likely point estimate of the primary random variable κ pertinent to porosity defects while providing a reduction in the variance of its distribution.
4. Principal component analysis was used to delineate salient aspects of the mechanical response of the aforementioned 2.5D BCC lattice structures. This involved characterization of auto-correlation functions of strain fields followed by their transformation to the Fourier space. The first two principal components could effectively classify defect-free lattice structures. However, this stark separation was found to collapse in presence of porosity defects, wherein projections pertaining to lattices featuring various strut thicknesses were found to cluster around closely spaced means. In comparison, analogous measures extracted from lattices with rough surfaces showed better separation in the space spanned by principal components produced from their response.
5. Analysis of the combined influence of porosity defect and surface roughness on the mechanical response of lattice structures suggested that these individual influences may be coupled multiplicatively in the Gibson-Ashby equation, especially if the presence of one family of defects does not alter the influence of another.
6. This work clearly suggests that the mechanical response of lattice structures is complicated by the presence of defects and surface roughness in a way that is intimately tied to attributes of the parent lattice itself. These linkages were not probed here in the context of other geometrical attributes such as lattice aspect ratio, lattice type, various modalities in spatial distributions of porosity defects, and wavelength spectrum of surface roughness, and this will be pursued in the near future.

5. Data availability

All data generated for research in this article is available upon request from the corresponding author. This is part of an ongoing project and we intend to upload all data and codes on open source repositories soon.

Declaration of Competing Interest

The authors declare that they have no known competing financial interests or personal relationships that could have appeared to influence the work reported in this paper.

Acknowledgements

SB would like to acknowledge partial support from NSF grant 1825686. Any opinions, findings, conclusions or recommendations expressed in this material are those of the authors and do not necessarily reflect the views of the National Science Foundation.

References

[1] C. Pleass, S. Jothi, Influence of powder characteristics and additive manufacturing process parameters on the microstructure and mechanical behaviour of inconel 625 fabricated by selective laser melting, Additive Manufacturing 24 (2018) 419–431.
[2] T. DebRoy, H. Wei, J.S. Zuback, T. Mukherjee, J.W. Elmer, J.O. Milewski, A. M. Beese, A.E. Wilson-Heid, A. De, W. Zhang, Additive manufacturing of metallic components-process, structure and properties, Progress in Materials Science 92 (2018) 112–224.
[3] M. Xia, D. Gu, G. Yu, D. Dai, H. Chen, Q. Shi, Porosity evolution and its thermodynamic mechanism of randomly packed powder-bed during selective laser melting of inconel 718 alloy, International Journal of Machine Tools and Manufacture 116.
[4] M. Leary, M. Mazur, H. Williams, E. Yang, A. Alghamdi, B. Lozanovski, X. Zhang, D. P. Shidid, L. Farahbod-Sternahl, G. Witt, I. Kelbassa, P. Choong, M. Qian, M. Brandt, Inconel 625 lattice structures manufactured by selective laser melting (slm): Mechanical properties, deformation and failure modes, Materials & Design 157.
[5] H.G. Salem, L.N. Carter, M.M.Attallah, Influence of processing parameters on internal porosity and types of defects formed in ti6al4v lattice structure fabricated by selective laser melting, Materials Science and Engineering: A 767.
[6] M. Zheng, L. Wei, J. Chen, Q. Zhang, C. Zhong, X. Lin, W. Huang, A novel method for the molten pool and porosity formation modelling in selective laser melting, International Journal of Heat and Mass Transfer 140.
[7] E. Hernández-Nava, C. Smith, F. Derguti, S. Tammas-Williams, F. Léonard, P. Withers, I. Todd, R. Goodall, The effect of defects on the mechanical response of ti-6al-4v cubic lattice structures fabricated by electron beam melting, Acta Materialia 108 (2016) 279–292.

[8] M. Suard, G. Martin, P. Lhuissier, R. Dendievel, F. Vignat, J.-J. Blandin, F. Villeneuve, Mechanical equivalent diameter of single struts for the stiffness prediction of lattice structures produced by electron beam melting, Additive Manufacturing 8 (2015) 124–131.
[9] S. Tammas-Williams, P.J. Withers, I. Todd, P.B. Prangnell, The effectiveness of hot isostatic pressing for closing porosity in titanium parts manufactured by selective electron beam melting, Metallurgical and Materials Transactions A 47 (5) (2016) 1939–1946.
[10] S. Tammas-Williams, P. Withers, I. Todd, P. Prangnell, Porosity regrowth during heat treatment of hot isostatically pressed additively manufactured titanium components, Scripta Materialia 122 (2016) 72–76.
[11] M. Kahlin, H. Ansell, D. Basu, A. Kerwin, L. Newton, B. Smith, J. Moverare, Improved fatigue strength of additively manufactured ti6al4v by surface post processing, International Journal of Fatigue 134 (2020), 105497.
[12] L. Liu, P. Kamm, F. García-Moreno, J. Banhart, D. Pasini, Elastic and failure response of imperfect three-dimensional metallic lattices: the role of geometric defects induced by selective laser melting, Journal of the Mechanics and Physics of Solids 107 (2017) 160–184, https://doi.org/10.1016/j.jmps.2017.07.003. URL: http://www.sciencedirect.com/science/article/pii/S0022509616307608.
[13] D. Li, R. Qin, B. Chen, J. Zhou, Analysis of mechanical properties of lattice structures with stochastic geometric defects in additive manufacturing, Materials Science and Engineering: A 141666 (2021).
[14] P.M. Khanolkar, C.C. McComb, S. Basu, Predicting elastic strain fields in defective microstructures using image colorization algorithms, Computational Materials Science 186 (2021), 110068.
[15] B.P. Croom, M. Berkson, R.K. Mueller, M. Presley, S. Storck, Deep learning prediction of stress fields in additively manufactured metals with intricate defect networks, arXiv preprint arXiv:2105.10564.
[16] A.G. Evans, J.W. Hutchinson, M.F. Ashby, Cellular metals, Current Opinion in Solid State and Materials Science 3.
[17] L.J. Gibson, M.F. Ashby, G. Schajer, C. Robertson, The mechanics of two-dimensional cellular materials, Proceedings of the Royal Society of London. A. Mathematical and Physical Sciences 382(1782) (1982) 25–42.
[18] I. Gibson, M.F. Ashby, The mechanics of three-dimensional cellular materials, Proceedings of the Royal Society of London. A. Mathematical and Physical Sciences 382(1782) (1982) 43–59.
[19] T. Maconachie, M. Leary, B. Lozanovski, X. Zhang, M. Qian, O. Faruque, M. Brandt, Slm lattice structures: Properties, performance, applications and challenges, Materials & Design 183 (2019), 108137.
[20] H. Salem, L. Carter, M. Attallah, H. Salem, Influence of processing parameters on internal porosity and types of defects formed in ti6al4v lattice structure fabricated by selective laser melting, Materials Science and Engineering: A 767 (2019), 138387.
[21] I. Torrano, O. Barbero, A. Kortabarria, P.J. Arrazola, Prediction of residual stresses in turning of Inconel 718, vol. 223, Trans Tech Publ, 2011.
[22] M. Beran, Statistical continuum theories, Transactions of the Society of Rheology 9 (1965) 339–355.
[23] I.T. Jolliffe, J. Cadima, Principal component analysis: a review and recent developments, Philosophical Transactions of the Royal Society A 374 (2016) 20150202.
[24] S.T. McKown, Y. Shen, W.K. Brookes, C. Sutcliffe, W.J. Cantwell, G.S. Langdon, G. N. Nurick, M.D. Theobald, The quasi-static and blast loading response of lattice structures, International Journal of Impact Engineering 35.
[25] A. Du Plessis, I. Yadroitsava, I. Yadroitsev, Effects of defects on mechanical properties in metal additive manufacturing: A review focusing on x-ray tomography insights, Materials & Design 187 (2020), 108385.
[26] N. Sanaei, A. Fatemi, N. Phan, Defect characteristics and analysis of their variability in metal l-pbf additive manufacturing, Materials & Design 182 (2019), 108091.
[27] S. Tammas-Williams, P.J. Withers, I. Todd, P. Prangnell, The influence of porosity on fatigue crack initiation in additively manufactured titanium components, Scientific Reports 7 (1) (2017) 1–13.
[28] Z. Xu, W. Wen, T. Zhai, Effects of pore position in depth on stress/strain concentration and fatigue crack initiation, Metallurgical and Materials Transactions A 43 (8) (2012) 2763–2770.
[29] H. Gong, K. Rafi, H. Gu, T. Starr, B. Stucker, Analysis of defect generation in ti–6al–4v parts made using powder bed fusion additive manufacturing processes, Additive Manufacturing 1 (2014) 87–98.
[30] L.-C. Zhang, Y. Liu, S. Li, Y. Hao, Additive manufacturing of titanium alloys by electron beam melting: a review, Advanced Engineering Materials 20 (5) (2018) 1700842.
[31] M.I. Hatamleh, J. Mahadevan, A. Malik, D. Qian, R. Kovacevic, Prediction of residual stress random fields for selective laser melted a357 aluminum alloy subjected to laser shock peening, Journal of Manufacturing Science and Engineering 141(10).
[32] A.W. Nelson, A.S. Malik, J.C. Wendel, M.E. Zipf, Probabilistic force prediction in cold sheet rolling by bayesian inference, Journal of Manufacturing Science and Engineering 136(4).